

Anomalous Lattice Effect Originated Metal-Insulator Transition in FeSe_x

Shubham Purwar,¹ Shinjini Paul,¹ Kritika Vijay,^{2,3} R. Venkatesh,⁴ Soma Banik,^{2,3} P. Mahadevan,¹ and S. Thirupathaiah^{1,*}

¹*Department of Condensed Matter and Materials Physics,*

S. N. Bose National Centre for Basic Sciences, Kolkata, West Bengal, India, 700106.

²*Accelerator Physics and Synchrotrons Utilization Division,*

Raja Ramanna Centre for Advanced Technology, Indore 452013, India

³*Homi Bhabha National Institute, Training School Complex, Anushakti Nagar, Mumbai, 400094, India*

⁴*UGC-DAE Consortium for Scientific Research, DAVV Campus, Indore 452001, MP, India.*

(Dated: January 23, 2025)

We present a comprehensive investigation of the structural, electrical transport, and magnetic properties of FeSe_x ($x = 1.14, 1.18, 1.23, 1.28, \text{ and } 1.32$) to unravel the mechanism of the metal-insulator transition observed in these systems. For this, we systematically evaluated the structural parameters of FeSe_x as a function of Se concentration and temperature. We observe increased lattice constants and cell volume with increased Se concentration. On the other hand, the temperature-dependent XRD studies suggest unusual lattice change around the metal-insulator (MI) transition temperature of the respective compositions. This remarkable observation suggests that the anomalous lattice effect originates the MI transition in these systems. Additionally, our density of states (DOS) calculations on $\text{FeSe}_{1.14}$ qualitatively explain the MI transition, as the low-temperature (50 K) structure DOS suggests a metallic nature and the high-temperature (300 K) structure DOS shows a gap near the Fermi level.

I. INTRODUCTION

Over the past decade, the iron-chalcogenides have captivated significant research interests due to their remarkable array of physical properties ranging from superconductivity to optical, thermal, and magnetic properties attributed to their diverse structural phases [1–3]. Also, the Fe-Se-based systems reveal a range of stable structural phases under ambient conditions, including FeSe_2 (orthorhombic), Fe_3Se_4 (monoclinic NiAs-type), Fe_7Se_8 (hexagonal NiAs-type), and FeSe (tetragonal PbO type) [4–6]. The physical properties of these Fe-Se-based systems span across metals, semiconductors, superconductors, and with varying magnetic structures from paramagnetic to ferrimagnetic, all influenced by the Fe/Se ratio present in the system [4–8]. These systems can be represented by the chemical formula FeSe_x ($x \geq 1$), exhibiting Fe-vacancy in their stable phases. For $x = 1 - 1.13$, FeSe_x adopts a PbO-type structure (α -phase), while for $x = 1.14 - 1.33$, it adopts a NiAs-type structure (β -phase) [9]. Further, a neutron diffraction study on $\text{FeSe}_{1.14}$ demonstrates that the in-plane Fe moments ferromagnetically order while the out-of-plane Fe moments orders antiferromagnetically, resulting in a ferrimagnetic system with a Néel temperature of 455 K, indicating a great potential for the room temperature spintronics applications [10].

In these systems, the Fe vacancies are typically ordered in alternating layers, leading to the formation of various superstructures such as 3c, 4c, 5c, and 6c, depending on the Fe or Se concentration [10–12]. In addition, $\text{FeSe}_{1.14}$ exhibits a spin-reorientation transition at around 100 K, where the easy axis of magnetization shifts from the ab-plane to the c-axis, causing a significant magnetocaloric effect over a

wide temperature range [13–15]. Mössbauer studies $\text{FeSe}_{1.14}$ suggest itinerant Fe 3d electrons [16], while its nanoscopic form exhibits giant coercivity, indicating a mixed valence state of Fe [17]. Interestingly, a metal-insulator transition at around 100 K has been reported earlier in the polycrystalline $\text{FeSe}_{1.14}$ from the electrical resistivity measurements that are ascribed to the spin-reorientation transition [6, 18]. On the other hand, the transport measurements on $\text{FeSe}_{1.14}$ single crystals having 3c superstructure indicate a metallic nature throughout the measured temperature range of 3–300 K without any MI transition [19, 20]. Another study demonstrates that the resistivity of $\text{FeSe}_{1.14}$ is metallic and temperature dependent below T_{SR} , but above T_{SR} it is temperature independent [12]. Thus, these systems' electrical transport properties, particularly the mechanism of metal-insulator transition, is still elusive. Interestingly, we prepared $\text{FeSe}_{1.14}$ composition that shows the spin-reorientation at around 100 K but the MI transition is found at around 250 K. This is in quite contrast to the previous reports on MI transition and spin-reorientation transitions found at around 100 K in these systems [6, 18]. This is surprising if one considers the spin-reorientation transition as the mechanism of MI transition as suggested earlier [6, 18]. Moreover, the recent studies on polycrystalline $\text{Fe}_{1.01-x}\text{Cu}_x\text{Se}$ and single crystalline $\text{Li}_x\text{Fe}_7\text{Se}_8$ suggest lattice disorder-originated MI transition [20–22]. Thus, the mechanism of metal-insulator transition in FeSe_x systems is yet to be clearly established.

In this manuscript, we aim at unravelling the mechanism of the metal-insulator transition observed in FeSe_x systems. In order to achieve this, we prepared polycrystalline FeSe_x compositions with various Se concentrations ($x = 1.14, 1.18, 1.23, 1.28, \text{ and } 1.32$) and performed a comprehensive investigation of the structural, electrical transport, and magnetic properties. Foremost, all these systems are found to crystallize in a trigonal crystal structure with a space group of $P3_121$. The structural analysis reveal that the lattice parameters (a(b) and c) show anomalous behaviour

* setti@bose.res.in

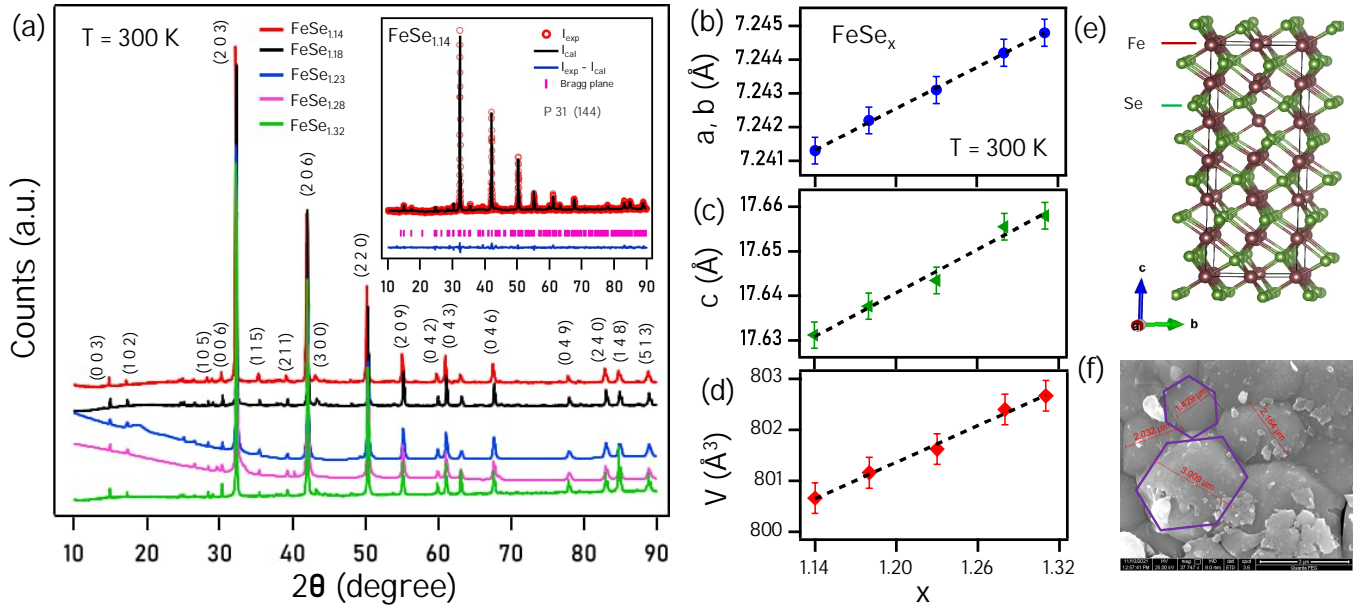


FIG. 1. (a) Powder X-ray diffraction (XRD) patterns of FeSe_x ($x = 1.14, 1.18, 1.23, 1.28,$ and 1.32) measured at room temperature. The inset in (a) shows Rietveld refinement of $\text{FeSe}_{1.14}$ XRD data. (b)–(d) Variation of lattice parameters ($a(b), c$) and unit cell volume (V) with selenium concentration (x). (e) Trigonal crystal structure of FeSe_x . (f) Scanning electron microscopy (SEM) image of the $\text{FeSe}_{1.14}$ pellet.

around the metal-insulator transition temperature within the temperature range of 185–279 K. Magnetic properties studies exhibit spin-reorientation transition within the temperature range 100–115 K, which is far away from the MI transition temperatures. This remarkable observation suggest an anomalous lattice effect-originated MI transition in these systems. To further confirm the structural-originated MI transition, we performed density functional theory (DFT) calculations using the lattice parameters obtained below and above the MI transition temperature. Our DFT calculations demonstrate reduction in the density of states near the Fermi level for the high-temperature structure (300 K) compared to the low-temperature (50 K) one. The temperature dependent valence band (VB) spectra measured using the photoemission spectroscopy also demonstrate the reduction in spectral density near the Fermi level with increasing temperature.

II. EXPERIMENTAL AND THEORETICAL DETAILS

A. Synthesis and Characterization Techniques

Polycrystalline FeSe_x with $x = 1.14, 1.18, 1.23, 1.28,$ and 1.32 were synthesized by the standard solid-state reaction method in evacuated quartz ampoule. In this method, the stoichiometric ratio of Iron (4N, Alfa Aesar) and Selenium powders (4N, Alfa Aesar) were weighed and ground thoroughly in an argon-filled glove box before sealing the mixture in an evacuated quartz ampoule. The quartz ampoule with the powder mixture was slowly heated up to 650°C for 10 hours and kept at this temperature for the next three days in a muffle furnace [11, 23]. After three days of reaction, the

ampoule was slowly cooled to room temperature. As-obtained final compositions were ground thoroughly again in an argon atmosphere, pressed using a two-torr pressure pelletizer, and then annealed at 650°C for two more days. All the prepared samples were stored in an argon-filled glove box to protect them from oxidation.

The phase purity of the compositions was examined by the X-ray diffraction (XRD) technique using a Rigaku X-ray diffractometer (SmartLab, 9kW) equipped with $\text{Cu K}\alpha$ radiation of wavelength 1.5406 \AA . The XRD measurements were performed within the temperature range of 3–300 K. Quantitative analysis of chemical compositions was performed using energy dispersive X-ray spectroscopy (EDS), and the morphology of crystallites was examined using the scanning electron microscope (SEM).

Electrical resistivity and magnetic measurements [$M(T)$ and $M(H)$] were carried out on the physical property measurement system (PPMS, 9 Tesla, Quantum Design-DynaCool). The electrical resistivity was measured in a standard four-probe method with an alternating current of 5 mA. Copper leads were attached to the sample using EPO-TEK H21D silver epoxy.

High-resolution X-ray photoelectron spectroscopy (XPS) measurements were conducted for the valence band (VB) spectra at 50 K (LT) and 300 K (HT) in Indus-2 synchrotron radiation centre at ARPES BL-10 beamline, equipped with PHOIBOS 150 electron analyzer. Atomically clean surface was achieved through argon ion sputtering at 1.5 keV for 1 hour. The valence band (VB) spectra were recorded using a photon energy of 75 eV with the energy resolution set at 30 meV for LT and 100 meV for RT. The measurement chamber vacuum was maintained at 7×10^{-11} mbar during the measurements.

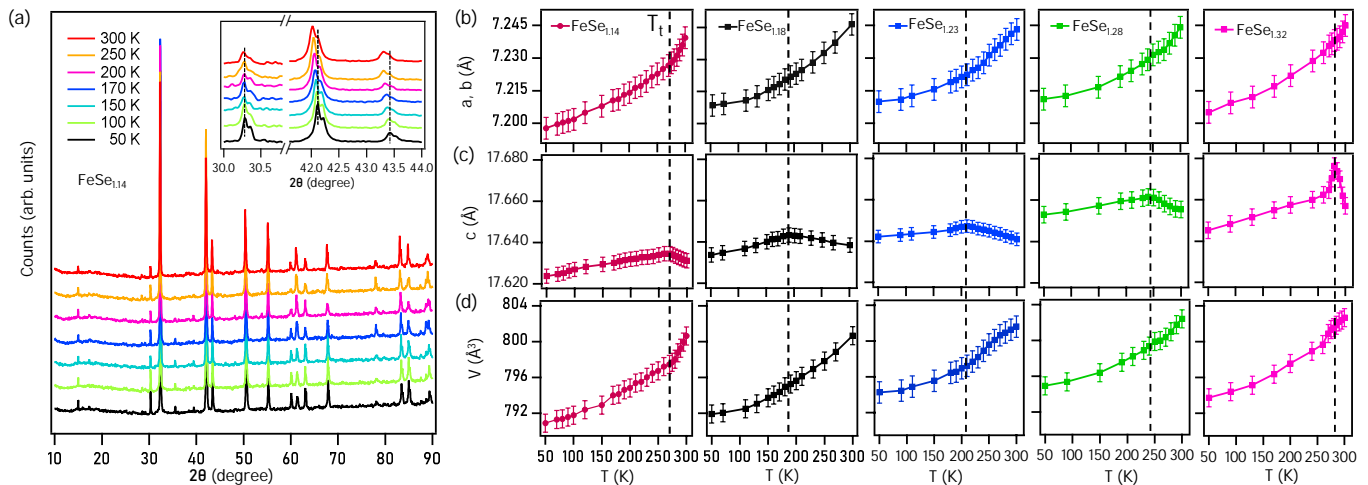


FIG. 2. (a) X-ray powder diffraction patterns were collected at different temperatures on $\text{FeSe}_{1.14}$. Inset in (a) shows the shift of (0 0 6) and (2 0 6) Bragg's peak positions with temperature. Temperature evolution of lattice parameters a (b) (b) and c (c). (d) Temperature evolution of unit cell volume (V). In the figure, T_t represents the anomalous lattice effect critical temperature for the respective samples.

B. Density Functional Theory

Electronic structure calculations were performed by density functional theory using plane-wave projected augmented basis set [24, 25] and generalized gradient approximation (GGA) exchange-correlation functional [26] as implemented in the Vienna Ab initio Simulation Package (VASP) [27–30]. In addition, orbital-dependent Coulomb interactions of 4 eV on the Fe 3d orbitals were included within the Dudarev implementation [31]. The experimental lattice parameters for the low-temperature structure at 50 K and the high-temperature structure at 300 K were used in the calculations, while the atoms were displaced till the forces on them were less than 5 meV/Å. A gamma-centered k-points grid of $6 \times 6 \times 3$ was used for the self-consistent calculations and a cutoff energy of 500 eV for the plane waves included in the basis. A k-point grid of $8 \times 8 \times 5$ points was used for further analysis of the electronic structure.

III. RESULTS AND DISCUSSION

A. Structural Properties

Figure 12(a) presents the room temperature X-ray diffraction (XRD) patterns for the iron selenide series FeSe_x with varying selenium concentrations ($x = 1.14, 1.18, 1.23, 1.28, \text{ and } 1.32$). The XRD analysis reveals that all diffraction peaks correspond to a pseudo-NiAs-type crystal structure, consistent with the trigonal $P3_121$ space group (No. 144), as previously reported [32]. Importantly, the absence of secondary phases, such as Fe_3Se_4 (monoclinic) [33], FeSe_2 (orthorhombic) [34], or FeSe (tetragonal) [35], confirms the phase purity of our synthesized compounds. A notable feature in the diffraction pattern is the (0 0 3) Bragg peak, attributed to iron vacancies within the lattice. These

vacancies are situated at specific crystallographic positions, namely $(1/2, 1/2, 0; 1/2, 0, 1/3; 0, 1/2, 2/3)$, which results in the formation of a $3c$ superstructure, as documented in earlier studies [11]. The inset of Fig. 12(a) shows the Rietveld refinement of the XRD data for $\text{FeSe}_{1.14}$ at 300 K, demonstrating an excellent agreement between the experimental data and the fitted model. Fig. S1 of the Supplemental Information details the Rietveld refinements for other compositions [36]. The derived lattice parameters and unit cell volumes for all compositions are summarized in Tab. ST1 of the Supplemental Information [36]. These values show a qualitative agreement with previously published data on these systems [4, 6, 11, 18, 37]. As shown in Fig. 12(b-d), increasing selenium concentration causes a monotonic expansion of the lattice constants and unit cell volume, likely due to additional lattice strain and increased Fe vacancy formation [38]. Fig. 12(e) illustrates the crystal structure of $\text{FeSe}_{1.14}$, featuring 21 Fe atoms and 24 Se atoms per unit cell. Fig. 12(f) presents a SEM image of $\text{FeSe}_{1.14}$, revealing hexagonal-shaped crystallites with typical sizes ranging from 4 to 9 μm^2 . SEM images for other compositions are provided in Fig. S2 of the Supplemental Information [36].

Intriguingly, we have also synthesized $\text{FeSe}_{1.38}$, which crystallizes in a monoclinic phase with the $C2/m$ space group, as shown in Fig. S6(a) of the Supplemental Information [36]. This suggests that the trigonal phase with the $3c$ superstructure is the only stable configuration within the FeSe_x series for $1.14 \leq x \leq 1.32$. This finding highlights a critical structural boundary within the FeSe_x system, where the stability of the trigonal phase is preserved up to a specific selenium concentration, beyond which a transition to the monoclinic phase occurs [5].

Figure 2 presents the temperature-dependent XRD patterns of $\text{FeSe}_{1.14}$ measured between 50 and 300 K. All patterns are indexed to the same trigonal crystal symmetry, with Bragg peaks shifting to higher diffraction angles as the temperature

increases, indicating the changes in the lattice parameters. The inset of Fig. 2(a) highlights this shift. No splitting of Bragg peaks was observed, suggesting the absence of a structural transition within this temperature range. Panels in Figs. 2(b) and 2(c) display the lattice constants $a(b)$ and c as a function of temperature for FeSe_x ($x = 1.14, 1.18, 1.23, 1.28, 1.32$), derived from Rietveld refinement. For $\text{FeSe}_{1.14}$, $a(b)$ increases linearly with temperature up to 260 K, after which it rapidly rises, while c increases linearly up to 260 K before decreasing. This indicates an unusual lattice behavior around a critical transition temperature of $T_t \approx 260$ K. Similar behaviors are observed in the other compositions at their respective critical transition temperatures ($T_t \approx 180$ K, 205 K, 245 K, and 275 K for $x = 1.18, 1.23, 1.28$, and 1.32, respectively). Despite these anomalies, the monotonic expansion of unit cell volume (V) with temperature, as shown in Fig. 2(d), suggests that elongation in the ab -plane dominates over contraction in the c direction [14]. Temperature-dependent XRD data for other Se concentrations are provided in Fig. S3 of Supplemental Information [36].

The anomalous lattice behaviour with temperature, as previously observed in other systems, is likely happening due to local structure distortions [37, 39, 40]. In iron chalcogenides, FeX_{1+y} ($X = \text{S}, \text{Se}$), the Fe cations octahedrally coordinates with six X anions to form FeX_6 octahedra. Whereas the X anions reside within trigonal prisms created by six Fe atoms, known as XFe_6 prisms [17, 41]. This arrangement harbors two distinct Fe ionic states (Fe^{2+} and Fe^{3+}), along with the Fe vacancies, leading complex structural behavior [11, 33]. In addition, the Fe 3d-orbitals split into threefold degenerate t_{2g} and twofold degenerate e_g states under the influence of crystal field splitting. The t_{2g} and e_g degeneracy are further lifted by the Jahn-Teller distortion, leading to additional symmetry breaking and new orbital energy levels [8]. This kind of structural reconfiguration is pivotal in influencing the material's physical properties. Furthermore, changes in the Fe-Fe bond length with temperature, as observed by I. Radelytskyi et al. in $\text{FeSe}_{1.14}$ (Fe_7Se_8), underscores the significance of temperature-dependent structural dynamics in these systems [14].

B. Magnetic Properties

Temperature-dependent magnetization ($M(T)$) of FeSe_x ($x = 1.14, 1.18, 1.23, 1.28$, and 1.32) is shown in Figs. 3(a)-3(e), measured with the zero-field-cooled (ZFC) and field-cooled (FC) modes under an applied magnetic field of 1000 Oe. Consistent with previous reports on $\text{FeSe}_{1.14}$, the spin-reorientation transition from the easy c -axis to easy ab -plane has been observed at $T_{\text{SR}} \approx 100$ K [see Fig. 3(a)], leading to an abrupt drop in the magnetization below T_{SR} [14]. The $T_{\text{SR}} \approx 100$ K also confirms the $3c$ superstructure present in the studied system [6, 10, 12, 18] as $T_{\text{SR}} \approx 220$ K is recorded for the $4c$ superstructure [42]. A similar spin-reorientation transition has been observed from the other Se concentration samples at their respective transition temperatures. Fig. 3(f)

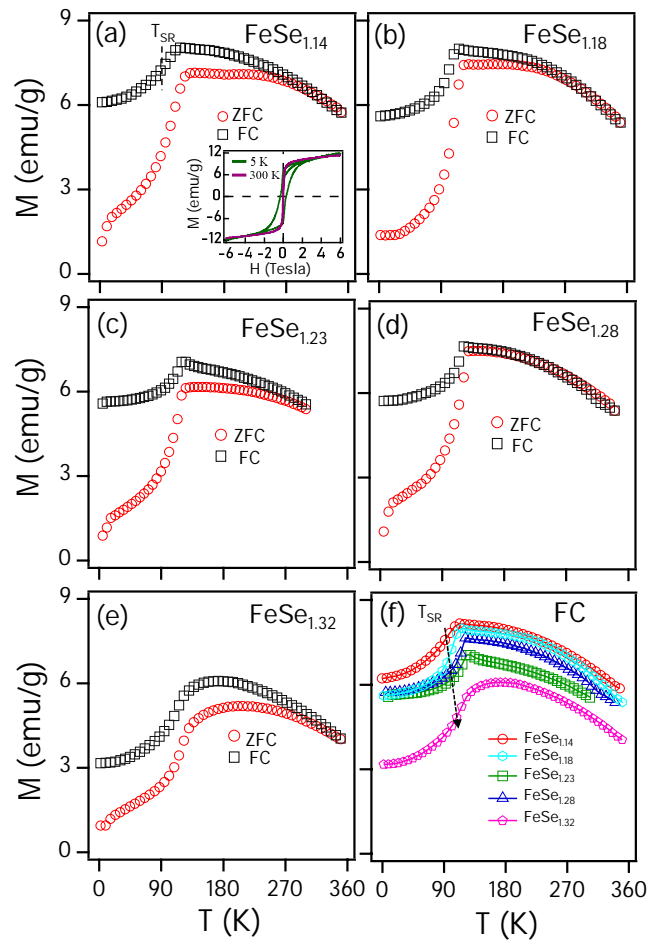


FIG. 3. (a)–(e) Temperature-dependent magnetization, $M(T)$, measured in zero-field cooled (ZFC) and field-cooled (FC) modes with an applied field of 1000 Oe for FeSe_x ($x = 1.14, 1.18, 1.23, 1.28$, and 1.32). The inset in (a) displays the magnetization as a function of field, $M(H)$, at $T = 5$ K and 300 K. In (a), T_{SR} represents the spin-reorientation transition, determined by dM/dT . (f) Comparison of temperature-dependent magnetization of FeSe_x compositions, demonstrating the evolution of T_{SR} with increasing x .

shows slight change in the spin-reorientation temperature with increasing Se concentration from $T_{\text{SR}} \approx 100$ K for $\text{FeSe}_{1.14}$ to $T_{\text{SR}} \approx 115$ K for $\text{FeSe}_{1.32}$. Further, the non-overlapping ZFC and FC curves and the magnetic hysteresis observed at 5 K suggest complex magnetic interactions in FeSe_x . This complexity arises from the coexistence of Fe^{2+} and Fe^{3+} states with ordered Fe vacancies [11, 43], leading to exchange, superexchange, and double exchange interactions [44].

To further investigate the magnetic state of FeSe_x , we plotted magnetization as a function of applied field [$M(H)$] in the inset of Fig. 3(a) for $\text{FeSe}_{1.14}$ measured at 5 and 300 K. The observed saturation magnetization (M_s) of $2.32 \mu_B/\text{f.u.}$ at 5 K aligns well with the previously reported values from similar systems [18]. $M(H)$ data for FeSe_x ($x = 1.18, 1.23, 1.28$, and 1.32) are shown in Fig. S4 of the Supplemental Information [36]. The magnetic hysteresis loop at 5 K exhibits

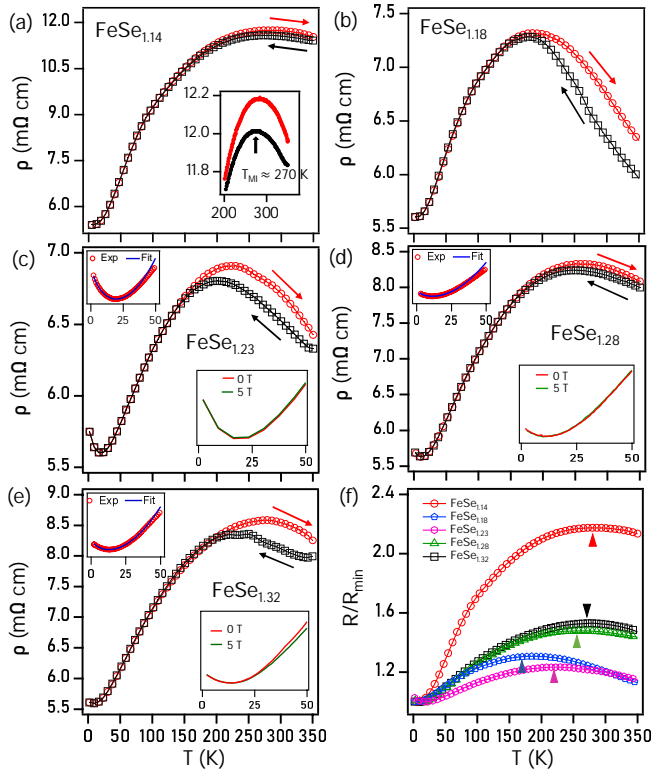


FIG. 4. (a)–(e) Temperature-dependent longitudinal electrical resistivity, $\rho(T)$, for polycrystalline FeSe_x ($x = 1.14, 1.18, 1.23, 1.28, \text{ and } 1.32$) measured from 2 to 350 K during both heating and cooling cycles. Inset in (a) demonstrates metal-insulator transition (T_{MI}) for $\text{FeSe}_{1.14}$. The top insets of (c), (d), and (e) show the low-temperature data fitted using the Eqn. 1. The bottom insets of (c), (d), and (e) display $\rho(T)$ under applied magnetic fields of $H = 0$ and 5 T. Panel (f) presents the normalized resistance measured during the heating cycle for FeSe_x . In (f), the arrows point the T_{MI} of various FeSe_x compositions.

a high coercive field (H_c) of 3000 Oe, consistent with previous observations in FeSe_x [6, 17], and the magnetization remains unsaturated up to 6 T, further confirming its ferrimagnetic nature at 5 K [8, 23, 45]. But at 300 K, despite the overall magnetic nature of the system is still the ferromagnetic, the magnetic hysteresis disappears.

C. Electrical Transport Properties

Figures 4(a)– 4(e) present the longitudinal electrical resistivity, $\rho(T)$, measured within the temperature range of 2 and 350 K for FeSe_x . The zoomed-in image shown in the inset of Fig. 4(a) demonstrates the metal-insulator transition temperature (T_{MI}) at approximately 270 K for $\text{FeSe}_{1.14}$. Similar metal-insulator transitions were observed from the other compositions as well at approximately 179 K, 198 K, 244 K, and 279 K, respectively, for $x = 1.18, 1.23, 1.28, \text{ and } 1.32$, as depicted in Fig. 4(f). Additionally, we detected thermal hysteresis near T_{MI} during the heating and cooling cycles of the resistivity measurements [see Figs. 4(a)–(e)],

underlining the structural changes around these temperatures. This is in agreement with the anomalous lattice behaviour observed in Figs. 2(b) and 2(c).

The metal-insulator transition, as observed in the resistivity data, can stem from various reasons, including the electron correlations [46, 47], structural phase transitions [48], or magnetic ordering [46, 48–50]. A subtle alteration in bond lengths, possibly driven by the Jahn-Teller effect, is also known to trigger the MI transitions [46, 51]. While changes in the crystal structure or the emergence of magnetic ordering, such as antiferromagnetism, can impact the electronic band structure, our observation of the decoupled spin-reorientation transitions eliminate the magnetism as the primary cause of the metal-insulator transition in FeSe_x systems. Instead, the anomalous behavior of temperature-dependent lattice parameters [a(b) and c] around T_t , coupled with significant thermal hysteresis near this transition, as depicted in Figs. 2 (b) and 4, strongly suggests that the structural distortions are the driving force of MI transition.

In addition to the T_{MI} transition, we observe an upturn in the electrical resistivity with a resistivity minima (T_m) at 20 K, 12 K, and 8.5 K for $\text{FeSe}_{1.23}$, $\text{FeSe}_{1.28}$, and $\text{FeSe}_{1.32}$, respectively. Such an upturn in the resistivity can arise from several reasons, including the Kondo effect [52], weak localization [52, 53], or the elastic electron-electron ($e-e$) scattering [54]. The Kondo effect typically occurs in nonmagnetic systems with diluted magnetic impurities [55], but given that all our samples are ordered, we can rule out this possibility. On the other hand, we perfectly fitted the upturn resistivity data using the inelastic $e-e$ scattering Eqn. 1 [54] as illustrated in the top inset of Figs. 4(c), 4(d), and 4(e). Thus, the upturn in the resistivity is predominantly driven by the elastic $e-e$ interactions, highlighting the electronic correlations in these systems. Fig. 4(f) shows normalized resistance as a function of temperature, demonstrating different T_{MI} for different Se concentrations.

$$\rho(T) = \rho_0 - \alpha * T^{0.5} + \beta * T^2 \quad (1)$$

where α and β are the elastic and inelastic $e-e$ scattering

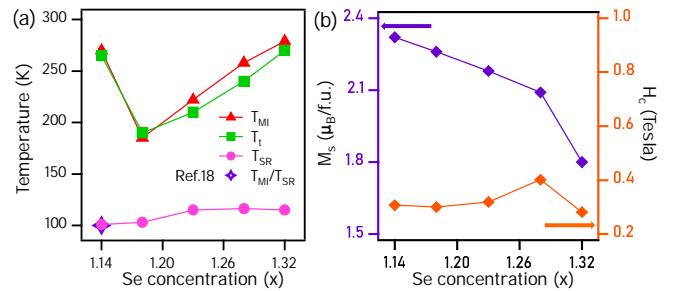


FIG. 5. (a) Spin-reorientation transition (T_{SR}), metal-insulator transition (T_{MI}), and anomalous lattice change (T_t) temperature are plotted as a function of Se concentration (x). (b) The saturation magnetization (H_s) and magnetic coercivity (H_c) are plotted as a function of Se concentration (x). Plots shown in this figure are summarized as tables in Tab. S2 and Tab. S3 of the Supplemental Information [36].

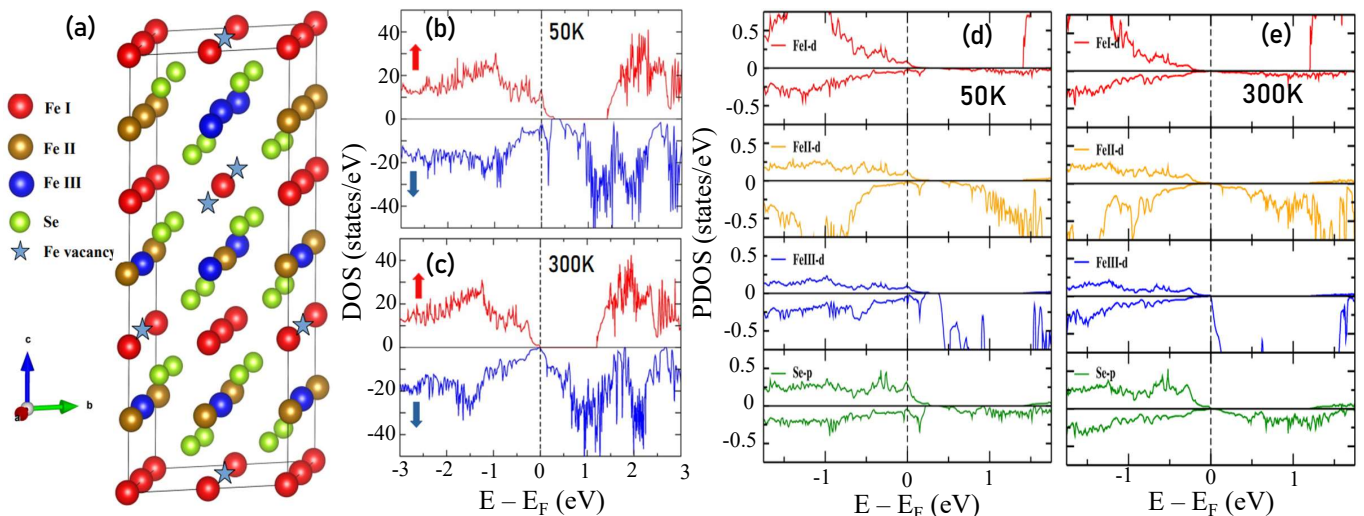


FIG. 6. The schematic presentation of the crystal structure of $\text{FeSe}_{1.14}$ illustrates the positions of various types of Fe (FeI, FeII, and FeIII) atoms and Fe vacancies. The total density of states (DOS) at 50 K (b) and 300 K (c) is shown with the red and blue lines representing the up-spin and down-spin channels, respectively. The projected DOS of the Fe 3d orbital contribution of each type of Fe (FeI, FeII, and FeIII) atoms and the Se 4p orbital contribution near Fe(II) are depicted at 50 K (d) and 300 K (e).

coefficients, respectively.

Next, Fig. 5(a) shows the spin-reorientation transition temperature (T_{SR}) plotted as a function of Se concentration (x). From Fig. 5(a), it is clear that T_{SR} slightly increases with increasing x , possibly due to the increase in the indirect exchange coupling strength [8]. On the other hand, T_{MI} shows a non-monotonic behaviour with increasing x and matches well with T_t (structural) transition, confirming that the metal-insulator transition is independent of magnetism [18]. Furthermore, as shown in Fig. 5(c), the saturation magnetization [M_s] extracted from Fig. 3 drops monotonically with increasing Se concentration, suggesting the robustness of direct exchange interaction (Fe-Fe) in these systems which decreases with increasing Se concentration. Remarkably, we also observe high coercivity H_c in these compounds at $T = 2$ K [see Fig. 5(d)] that is almost independent of Se concentration.

IV. ELECTRONIC BAND STRUCTURE

We examined the temperature-dependent changes in the electronic structure of $\text{FeSe}_{1.14}$ by calculating the density of states for the 50 K and 300 K using the lattice parameters determined at these respective temperatures. Our calculations confirm that the ferrimagnetic state has the lowest ground state energy in which the in-plane spins align in parallel. At the same time, they are oriented antiparallel in the out-of-plane direction, considering the layer stacking in the c -direction. We observe three types of magnetic moments of Fe in the system on the basis of their positions. The Fe atoms in the layers that contain the Fe vacancies are denoted as FeI and are situated between vacancy-free Fe layers in which the atoms are classified as FeII (far from the vacancy) and FeIII (near to the vacancy) as shown in Fig. 6(a). The magnetic moments

on Fe are found to be $3.37 \mu_B$ for FeI, $3.52 \mu_B$ for FeII, and $3.76 \mu_B$ for FeIII from the high-temperature structure, while for the low-temperature structure they are 3.37 , 3.49 and $3.76 \mu_B$, respectively. Hence, the structural changes lead to a small change in the magnetic moment of the FeII atom. However, the effect of structural change is found to be significant on the electronic band structure.

Fig. 6(b) shows the spin-polarized density of states calculated for the 50 K temperature structure, while Fig. 6(c) shows the same but calculated for the 300 K structure. Specifically, the low-temperature structure is found to be metallic, while a gap opens up in the density of states associated with the high-temperature structure as shown in Figs. 6(b) and 6(c). To understand the changes in the electronic structure due to structural modifications, we examined the projected partial density of states for the FeI, FeII, FeIII 3d, and Se 4p states shown in Figs. 6(d) and 6(e). In the partial density of states, we observe that Fe has almost fully occupied up-spin and partially occupied down-spin states in each case. As the lattice parameter (a , b) of the structure increases with temperature, an overall increase in Fe-Se bond length in going from the low-temperature structure to the high-temperature structure is observed. An increase in the Fe-Se bond length decreases the Fe-Se hopping interaction strength, pulling the anti-bonding states deeper into the valence band and thus driving the system to an insulating state at high temperatures.

We further measured the valence band spectra using the X-ray photoelectron spectroscopy (XPS) using 75 eV photon energy on $\text{FeSe}_{1.14}$ at various temperatures as shown in Fig. 7. In Fig. 7, we also compared the experimental spectral features measured at 50, 100 and 300 K with the calculated density of states (DOS) for the structures at respective temperatures. Although the photoemission cross-section of Fe 3d is approximately 47 times greater

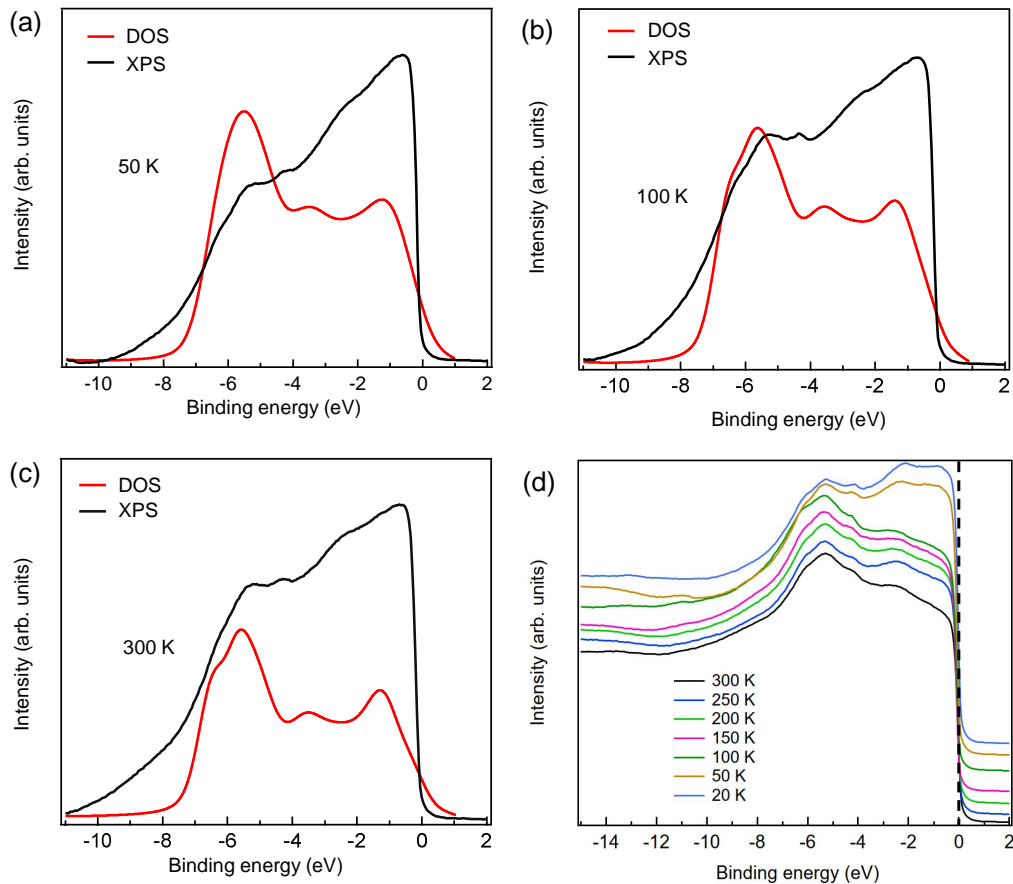


FIG. 7. X-ray photoelectron spectroscopy (XPS) measurements on $\text{FeSe}_{1.14}$. (a)-(c) Calculated density of states (DOS) overlapped with valence band (VB) spectra obtained using XPS. (d) Temperature-dependent valence band spectra. The data in (d) is offset vertically for a better visualization. In figure, the VB spectra is measured with a photon energy of 75 eV.

than that of Se 4p at a photon energy of 75 eV [56], the peak positions in both the XPS and DOS data show good agreement. Thus, the experimental valence band spectra support the theoretical prediction of changes in the density of states between the high and low-temperature structures. In addition, from the temperature dependent valence band spectra [see Fig. 7(d)], we notice that the spectral intensity near the Fermi level decreases drastically with increasing temperature when compared to the spectral intensity below Fermi level ($E = -2.5$ eV and -5.7 eV), further supporting the metal-insulator transition observed at the high temperatures as the states near the Fermi level contribute to the electrical transport. Finally, before the conclusion, we would like to highlight the electrical transport and magnetization data of monoclinic $\text{FeSe}_{1.38}$ as shown in Fig. S5 of the Supplemental Information [36]. Interestingly, in Fig. S5(b), we do not find any MI transition in the resistivity data between 2 and 350 K despite the magnetization data clearly showing the spin-reorientation transition at around 112 K. This further supports our argument on the non-magnetic originated MI transition in these systems.

V. SUMMARY

In summary, we investigated the metal-insulator (MI) transition in FeSe_x by synthesizing the polycrystalline samples with varying selenium concentrations ($x = 1.14, 1.18, 1.23, 1.28, \text{ and } 1.32$) and performing a comprehensive analysis on their structural, electrical, and magnetic properties. All samples exhibit a trigonal crystal structure with the $P3_121$ space group. Magnetization studies reveal a spin-reorientation transition, varying between 100-116 K, that is decoupled with the MI transition, varying between 185 and 279 K. On the other hand, the temperature-dependent XRD studies suggest unusual lattice changes around the metal-insulator (MI) transition temperature of the respective compositions, T_t varying between 190 and 280 K. This remarkable observation suggests that the anomalous lattice effect originates the MI transition in these systems. Additionally, our density of states (DOS) calculations on $\text{FeSe}_{1.14}$ at 50 K and 300 K qualitatively explain the MI transition, as the low-temperature (50 K) structure DOS suggests a metallic nature and the high-temperature (300 K) structure DOS shows a gap near the Fermi level.

VI. ACKNOWLEDGEMENT

This research has used the Technical Research Centre (TRC) Instrument Facilities of S. N. Bose National Centre for Basic Sciences, established under the TRC project of the Department of Science and Technology. P.M. acknowledges the support from SERB through Project

No. SERBPOWER(SPF/2021/000066). The support and the resources provided by Param Yukti Facility under the National Supercomputing Mission, Government of India at the Jawaharlal Nehru Centre For Advanced Scientific Research, Bengaluru are gratefully acknowledged. S.Paul acknowledges the PhD fellowship from DST-INSPIRE(IF190524), Government of India.

-
- [1] F.-C. Hsu, J.-Y. Luo, K.-W. Yeh, T.-K. Chen, T.-W. Huang, P. M. Wu, Y.-C. Lee, Y.-L. Huang, Y.-Y. Chu, D.-C. Yan, *et al.*, Superconductivity in the PbO-type structure α -FeSe, *Proceedings of the National Academy of Sciences* **105**, 14262 (2008).
- [2] D. Hu, C. Ye, X. Wang, X. Zhao, L. Kang, J. Liu, R. Duan, X. Cao, Y. He, J. Hu, *et al.*, Chemical vapor deposition of superconducting $\text{FeTe}_{1-x}\text{Se}_x$ nanosheets, *Nano Letters* **21**, 5338 (2021).
- [3] J. Xu, W. Li, B. Zhang, L. Zha, W. Hao, S. Hu, J. Yang, S. Li, S. Gao, and Y. Hou, Free-standing 2d non-van der waals antiferromagnetic hexagonal FeSe semiconductor: halide-assisted chemical synthesis and Fe^{2+} related magnetic transitions, *Chemical Science* **13**, 203 (2022).
- [4] A. Okazaki and K. Hirakawa, Structural study of iron selenides FeSe_x . i ordered arrangement of defects of Fe atoms, *Journal of the Physical Society of Japan* **11**, 930 (1956).
- [5] G. C. Tewari, D. Srivastava, R. Pohjonen, O. Mustonen, A. J. Karttunen, J. Lindén, and M. Karppinen, Fe_3Se_4 : a possible ferrimagnetic half-metal?, *Journal of Physics: Condensed Matter* **32**, 455801 (2020).
- [6] Z. Zhao, J. Zhou, L. Liu, N. Liu, J. Huang, B. Zhang, W. Li, Y. Zeng, T. Zhang, W. Ji, *et al.*, Two-dimensional room-temperature magnetic nonstoichiometric Fe_7Se_8 nanocrystals: Controllable synthesis and magnetic behavior, *Nano Letters* **22**, 1242 (2022).
- [7] D. Liu, W. Zhang, D. Mou, J. He, Y.-B. Ou, Q.-Y. Wang, Z. Li, L. Wang, L. Zhao, S. He, *et al.*, Electronic origin of high-temperature superconductivity in single-layer FeSe superconductor, *Nature communications* **3**, 931 (2012).
- [8] M. Ghalawat and P. Poddar, Remarkable effect of Fe and Se composition on magnetic properties comparative study of the Fe–Se system at the nanoscale, *The Journal of Physical Chemistry C* **126**, 4655 (2022).
- [9] G. Hägg and A.-L. Kindström, Röntgenuntersuchung am system eisen—selen, *Zeitschrift für Physikalische Chemie* **22**, 453 (1933).
- [10] M. Kawaminami and A. Okazaki, Neutron diffraction study of Fe_7Se_8 . ii, *Journal of the physical Society of Japan* **29**, 649 (1970).
- [11] A. Andresen, , and J. Leciejewicz, A neutron diffraction study of Fe_7Se_8 , *Journal de Physique* **25**, 574 (1964).
- [12] M. Kawaminami and A. Okazaki, Neutron diffraction study of Fe_7Se_8 , *Journal of the Physical Society of Japan* **22**, 924 (1967).
- [13] K. Adachi and K. Sato, Origin of magnetic anisotropy energy of Fe_7S_8 and Fe_7Se_8 , *Journal of Applied Physics* **39**, 1343 (1968).
- [14] I. Radelytskyi, P. Aleshkevych, D. Gawryluk, M. Berkowski, T. Zajarniuk, A. Szewczyk, M. Gutowska, L. Hawelek, P. Włodarczyk, J. Fink-Finowicki, *et al.*, Structural, magnetic, and magnetocaloric properties of Fe_7Se_8 single crystals, *Journal of applied physics* **124**, 143902 (2018).
- [15] Y. Konopelyk, I. Radelytskyi, P. Iwanowski, D. Gawryluk, M. Berkowski, R. Diduszko, J. Fink-Finowicki, H. Szymczak, and R. Puzniak, Combined pressure and magnetic-field induced caloric effects in Fe_7Se_8 single crystals, *Journal of Magnetism and Magnetic Materials* **543**, 168626 (2022).
- [16] H. N. Ok, K. S. Baek, and E. C. Kim, Mossbauer study of “3c” superstructure of the ferrimagnetic Fe_7Se_8 , *Solid state communications* **87**, 1169 (1993).
- [17] I. Lyubutin, C.-R. Lin, K. Funtov, T. Dmitrieva, S. Starchikov, Y.-J. Siao, and M.-L. Chen, Structural, magnetic, and electronic properties of iron selenide $\text{Fe}_{6-7}\text{Se}_8$ nanoparticles obtained by thermal decomposition in high-temperature organic solvents, *The Journal of chemical physics* **141**, 044704 (2014).
- [18] G. Li, B. Zhang, T. Baluyan, J. Rao, J. Wu, A. A. Novakova, P. Rudolf, G. R. Blake, R. A. de Groot, and T. T. Palstra, Metal–insulator transition induced by spin reorientation in Fe_7Se_8 grain boundaries, *Inorganic chemistry* **55**, 12912 (2016).
- [19] A. Pajaczkowska, P. Peshev, M. Ivanova, and R. Gałazka, On the preparation of Fe_7Se_8 single crystals by a chemical transport reaction, *Materials Research Bulletin* **9**, 1267 (1974).
- [20] T. Ying, Y. Gu, X. Chen, X. Wang, S. Jin, L. Zhao, W. Zhang, and X. Chen, Anderson localization of electrons in single crystals: $\text{Li}_x\text{Fe}_7\text{Se}_8$, *Science advances* **2**, e1501283 (2016).
- [21] P. W. Anderson, Absence of diffusion in certain random lattices, *Phys. Rev.* **109**, 1492 (1958).
- [22] S. Chadov, D. Schärff, G. H. Fecher, C. Felser, L. Zhang, and D. J. Singh, Electronic structure, localization, and spin-state transition in cu-substituted $\text{FeSe} : \text{Fe}_{1-x}\text{Cu}_x\text{Se}$, *Phys. Rev. B* **81**, 104523 (2010).
- [23] D. Akramov, N. Selezneva, P. Ibrahim, V. Maikov, E. Sherokalova, D. Kuznetsov, and N. Baranov, Effect of milling on the magnetic properties of the Fe_7S_8 and Fe_7Se_8 compounds, *Physics of Metals and Metallography* **123**, 282 (2022).
- [24] P. E. Blöchl, Projector augmented-wave method, *Phys. Rev. B* **50**, 17953 (1994).
- [25] G. Kresse and D. Joubert, From ultrasoft pseudopotentials to the projector augmented-wave method, *Phys. Rev. B* **59**, 1758 (1999).
- [26] J. P. Perdew, K. Burke, and M. Ernzerhof, Generalized gradient approximation made simple, *Phys. Rev. Lett.* **77**, 3865 (1996).
- [27] G. Kresse and J. Furthmüller, Efficient iterative schemes for ab initio total-energy calculations using a plane-wave basis set, *Phys. Rev. B* **54**, 11169 (1996).
- [28] G. Kresse and J. Furthmüller, Efficiency of ab-initio total energy calculations for metals and semiconductors using a plane-wave basis set, *Computational materials science* **6**, 15 (1996).
- [29] G. Kresse and J. Hafner, Ab initio molecular dynamics for liquid metals, *Phys. Rev. B* **47**, 558 (1993).

- [30] G. Kresse and J. Hafner, Ab initio molecular-dynamics simulation of the liquid-metal–amorphous-semiconductor transition in germanium, *Phys. Rev. B* **49**, 14251 (1994).
- [31] S. L. Dudarev, G. A. Botton, S. Y. Savrasov, C. J. Humphreys, and A. P. Sutton, Electron-energy-loss spectra and the structural stability of nickel oxide: An lsda+u study, *Phys. Rev. B* **57**, 1505 (1998).
- [32] S. B. Harris and R. P. Camata, X-ray diffraction data and analysis to support phase identification in fese and Fe₇Se₈ epitaxial thin films, *Data in brief* **27**, 104778 (2019).
- [33] A. Andresen, A neutron diffraction investigation of Fe₃Se₄, *ACTA CHEM SCAND* **22**, 827 (1968).
- [34] B. Lavina, R. T. Downs, and S. Sinogeikin, The structure of ferroselite, FeSe₂, at pressures up to 46 gpa and temperatures down to 50 k: A single-crystal micro-diffraction analysis, *Crystals* **8**, 289 (2018).
- [35] J. N. Millican, D. Phelan, E. L. Thomas, J. B. Leão, and E. Carpenter, Pressure-induced effects on the structure of the FeSe superconductor, *Solid State Communications* **149**, 707 (2009).
- [36] Supplemental Information can be found at..
- [37] A. Okazaki, The superstructures of iron selenide Fe₇Se₈, *Journal of the physical Society of Japan* **16**, 1162 (1961).
- [38] A. R. Denton and N. W. Ashcroft, Vegard's law, *Phys. Rev. A* **43**, 3161 (1991).
- [39] D. Louca and T. Egami, Lattice effect in the metal-insulator transition in cmr manganites, *Physica B: Condensed Matter* **241**, 842 (1997).
- [40] V. Petkov, T. D. Rao, A. Zafar, A. M. Abeykoon, E. Fletcher, J. Peng, Z. Mao, and X. Ke, Lattice distortions and the metal-insulator transition in pure and ti-substituted Ca₃Ru₂O₇, *Journal of Physics: Condensed Matter* **51**, 015402 (2022).
- [41] A. Wold and K. Dwight, *Solid State Chemistry* (Springer Science and Business Media, 1993).
- [42] P. Terzieff and K. L. Komarek, The antiferromagnetic and ferrimagnetic properties of iron selenides with nias-type structure, *Monatshefte für Chemie/Chemical Monthly* **109**, 1037 (1978).
- [43] C.-R. Lin, Y.-J. Siao, S.-Z. Lu, and C. Gau, Magnetic properties of iron selenide nanocrystals synthesized by the thermal decomposition, *IEEE Transactions on Magnetics* **45**, 4275 (2009).
- [44] X. Zhang, B. Wang, Y. Guo, Y. Zhang, Y. Chen, and J. Wang, High curie temperature and intrinsic ferromagnetic half-metallicity in two-dimensional Cr₃X₄ (x = s, se, te) nanosheets, *Nanoscale Horizons* **4**, 859 (2019).
- [45] M.-R. Gao, Z.-Y. Lin, J. Jiang, H.-B. Yao, Y.-M. Lu, Q. Gao, W.-T. Yao, and S.-H. Yu, Selective synthesis of Fe₇Se₈ polyhedra with exposed high-index facets and Fe₇Se₈ nanorods by a solvothermal process in a binary solution and their collective intrinsic properties, *Chemistry—A European Journal* **17**, 5068 (2011).
- [46] V. Kiryukhin, D. Casa, J. Hill, B. Keimer, A. Vigliante, Y. Tomioka, and Y. Tokura, An x-ray-induced insulator–metal transition in a magnetoresistive manganite, *Nature* **386**, 813 (1997).
- [47] C. Lee, H. Matsuhata, A. Yamamoto, T. Ohta, H. Takazawa, K. Ueno, C. Sekine, I. Shirotni, and T. Hirayama, Structural phase transition accompanied by metal-insulator transition in PrRu₄P₁₂, *Journal of Physics: Condensed Matter* **13**, L45 (2001).
- [48] J. Dho, W. S. Kim, and N. H. Hur, Anomalous thermal hysteresis in magnetization and resistivity of La_{1-x}Sr_xMnO₃, *Phys. Rev. Lett.* **87**, 187201 (2001).
- [49] M. Imada, A. Fujimori, and Y. Tokura, Metal-insulator transitions, *Rev. Mod. Phys.* **70**, 1039 (1998).
- [50] R. D. Sanchez, M. Causa, A. Seoane, J. Rivas, F. Rivadulla, M. López-Quintela, J. P. Cacho, J. Blasco, and J. Garcia, Metal-insulator transition and magnetic properties of La_{1-x}Eu_xNiO₃ (0 ≤ x ≤ 1), *Journal of Solid State Chemistry* **151**, 1 (2000).
- [51] J. L. Garcia-Munoz, J. Rodríguez-Carvajal, P. Lacorre, and J. B. Torrance, Neutron-diffraction study of RNiO₃ (r=la, pr, nd, sm): Electronically induced structural changes across the metal-insulator transition, *Phys. Rev. B* **46**, 4414 (1992).
- [52] S. Dhara, R. R. Chowdhury, and B. Bandyopadhyay, Observation of resistivity minimum at low temperature in Co_xCu_{1-x} (x ~ 0.17–0.76) nanostructured granular alloys, *Phys. Rev. B* **93**, 214413 (2016).
- [53] B. L. Altshuler, D. Khmel'nitzkii, A. I. Larkin, and P. A. Lee, Magnetoresistance and hall effect in a disordered two-dimensional electron gas, *Phys. Rev. B* **22**, 5142 (1980).
- [54] E. Guo, L. Wang, Z. Wu, L. Wang, H. Lu, K. Jin, and J. Gao, Magnetic field mediated low-temperature resistivity upturn in electron-doped La_{1-x}Hf_xMnO₃ manganite oxides, *Journal of Applied Physics* **112**, 123710 (2012).
- [55] S. Barua, M. C. Hatnean, M. Lees, and G. Balakrishnan, Signatures of the kondo effect in VSe₂, *Scientific reports* **7**, 10964 (2017).
- [56] J. Yeh and I. Lindau, Atomic subshell photoionization cross sections and asymmetry parameters: 1 ≤ z ≤ 103, *Atomic data and nuclear data tables* **32**, 1 (1985).

SUPPLEMENTARY INFORMATION

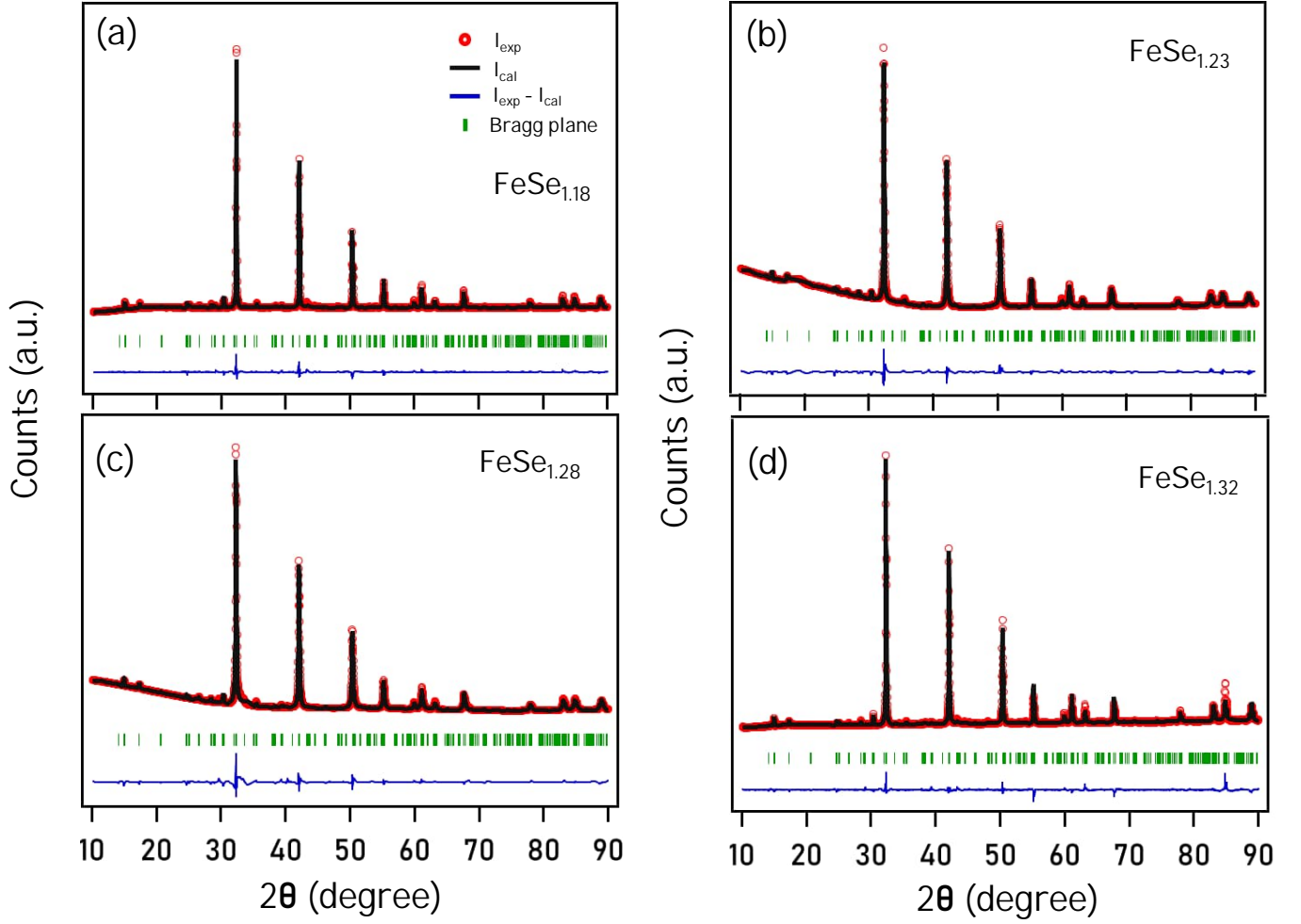


FIG. 8. Fig. S1: Room temperature X-ray diffraction patterns of FeSe_x with $x = 1.18, 1.23, 1.28,$ and 1.32 . Rietveld refinement confirms that all diffraction peaks correspond to the trigonal phase with no detectable impurity phases.

TABLE I. Tab S1: Summary of the structural parameters of FeSe_x

Composition	a, b (Å)	c (Å)	V (Å ³)	χ^2
$\text{FeSe}_{1.14}$	7.2413(3)	17.6312(4)	800.661(2)	2.64
$\text{FeSe}_{1.18}$	7.2422(4)	17.6377(6)	801.158(4)	3.01
$\text{FeSe}_{1.23}$	7.2431(3)	17.6435(3)	801.62(4)	3.44
$\text{FeSe}_{1.28}$	7.2442(5)	17.6555(4)	802.402(2)	4.53
$\text{FeSe}_{1.32}$	7.2448(4)	17.6580(3)	802.665(4)	5.03

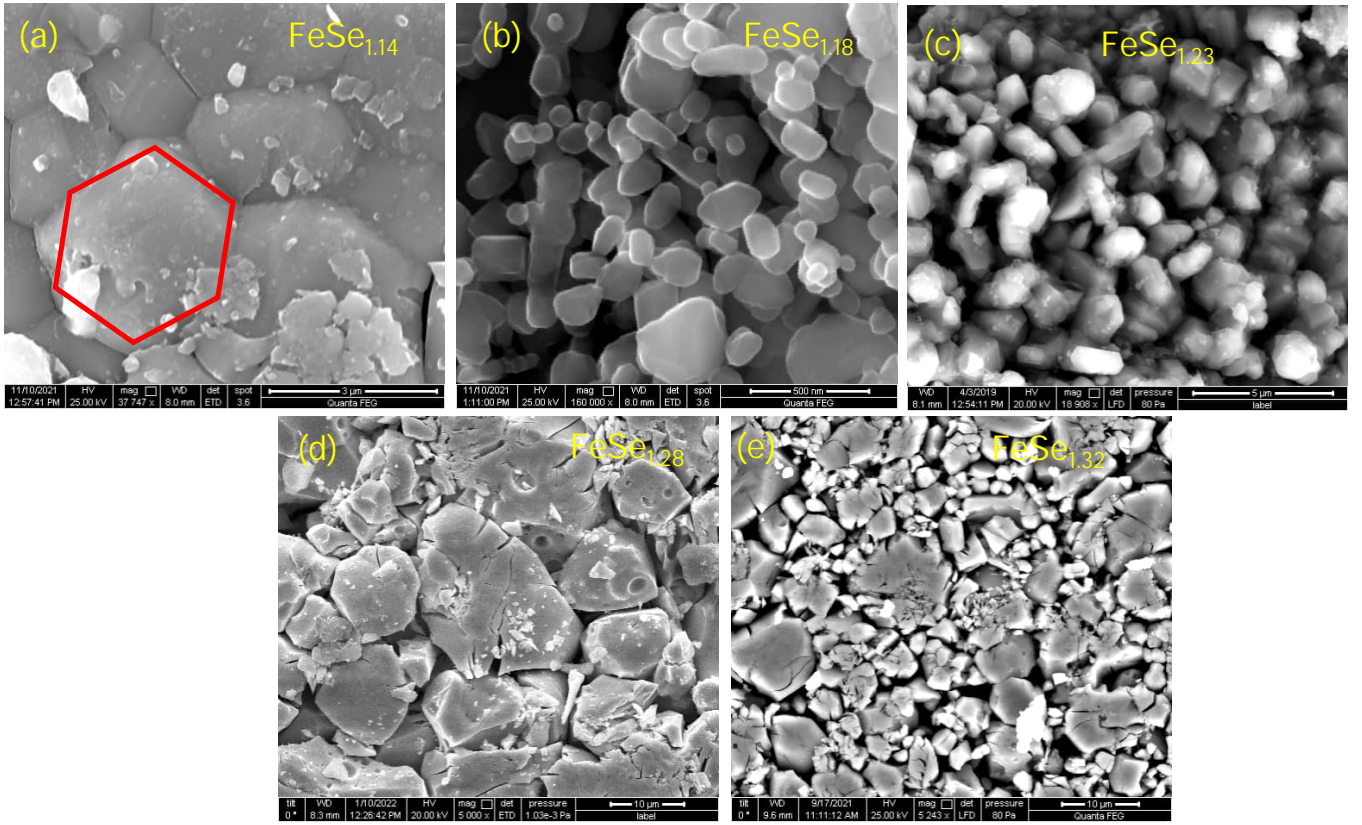


FIG. 9. Fig. S2:Field Emission Scanning Electron Microscopy (FE-SEM) images of trigonal FeSe_x with $x = 1.14, 1.18, 1.23, 1.28,$ and 1.32 .

TABLE II. Tab S2: Summary of metal-insulator transition (T_{MI}), Spin-reorientation transition (T_{SR}), anomalous lattice effect temperature (T_t), and low-temperature minima due to Coulombic interactions (T_{CI}).

Composition	T_{MI} (K)	T_{SR} (K)	T_t (K)	T_{CI} (K)
$\text{FeSe}_{1.14}$	270	101	265	
$\text{FeSe}_{1.18}$	185	103	190	
$\text{FeSe}_{1.23}$	222	115	210	20
$\text{FeSe}_{1.28}$	258	116	240	12
$\text{FeSe}_{1.32}$	279	115	280	8.5

TABLE III. Tab S3: Summary of saturation magnetization (M_s) and coercivity (H_c) at 5 K.

Composition	H_c (Oe)	M_s ($\mu_B/\text{f.u.}$)
$\text{FeSe}_{1.14}$	3071.6	2.32
$\text{FeSe}_{1.18}$	3000	2.26
$\text{FeSe}_{1.23}$	3188.3	2.18
$\text{FeSe}_{1.28}$	4015	2.09
$\text{FeSe}_{1.32}$	2813.2	1.8

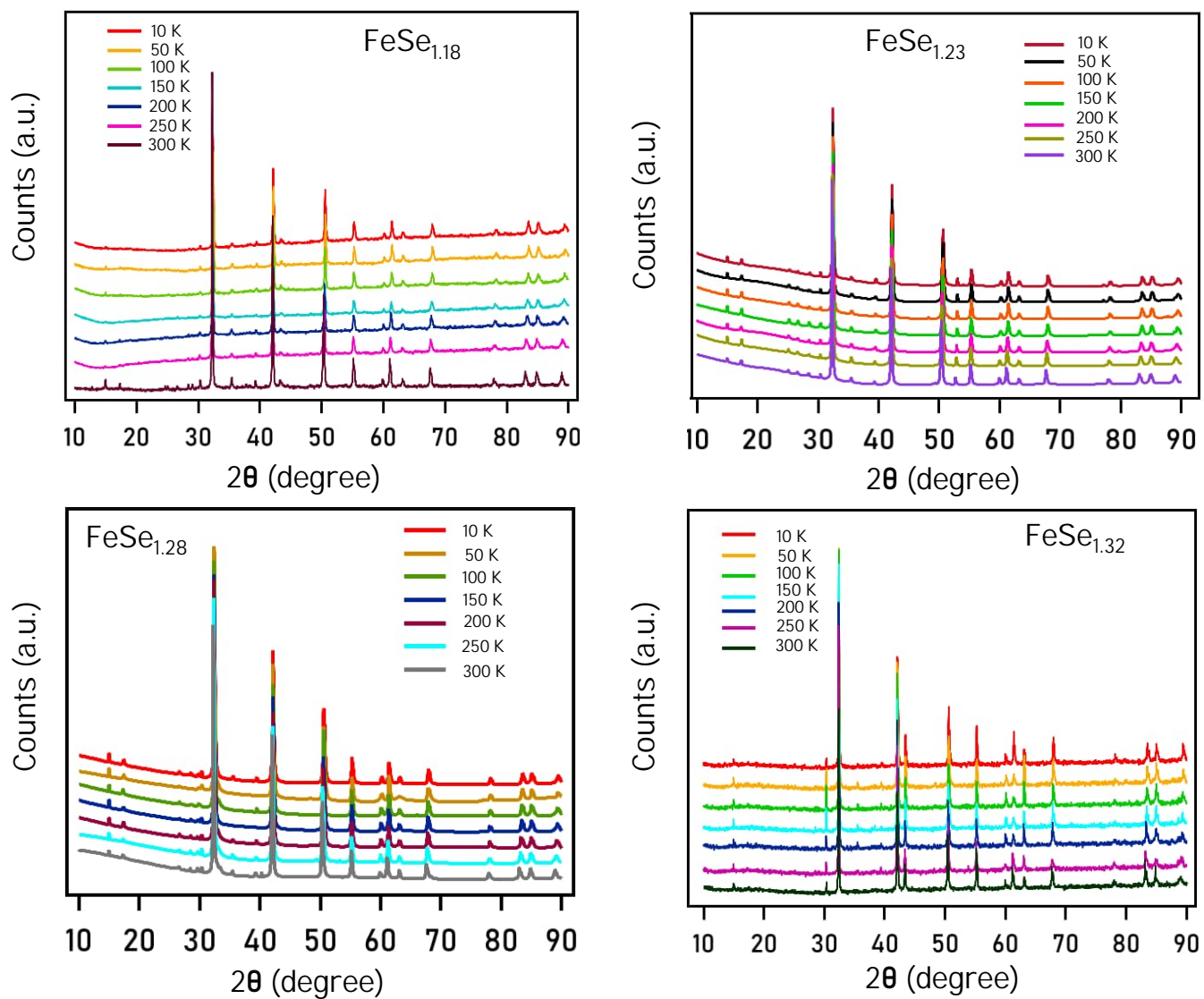


FIG. 10. Fig. S3: Temperature-dependent X-ray diffraction (XRD) patterns of FeSe_x for $x = 1.18, 1.23, 1.28,$ and 1.32 , recorded across the temperature range of 10–300 K.

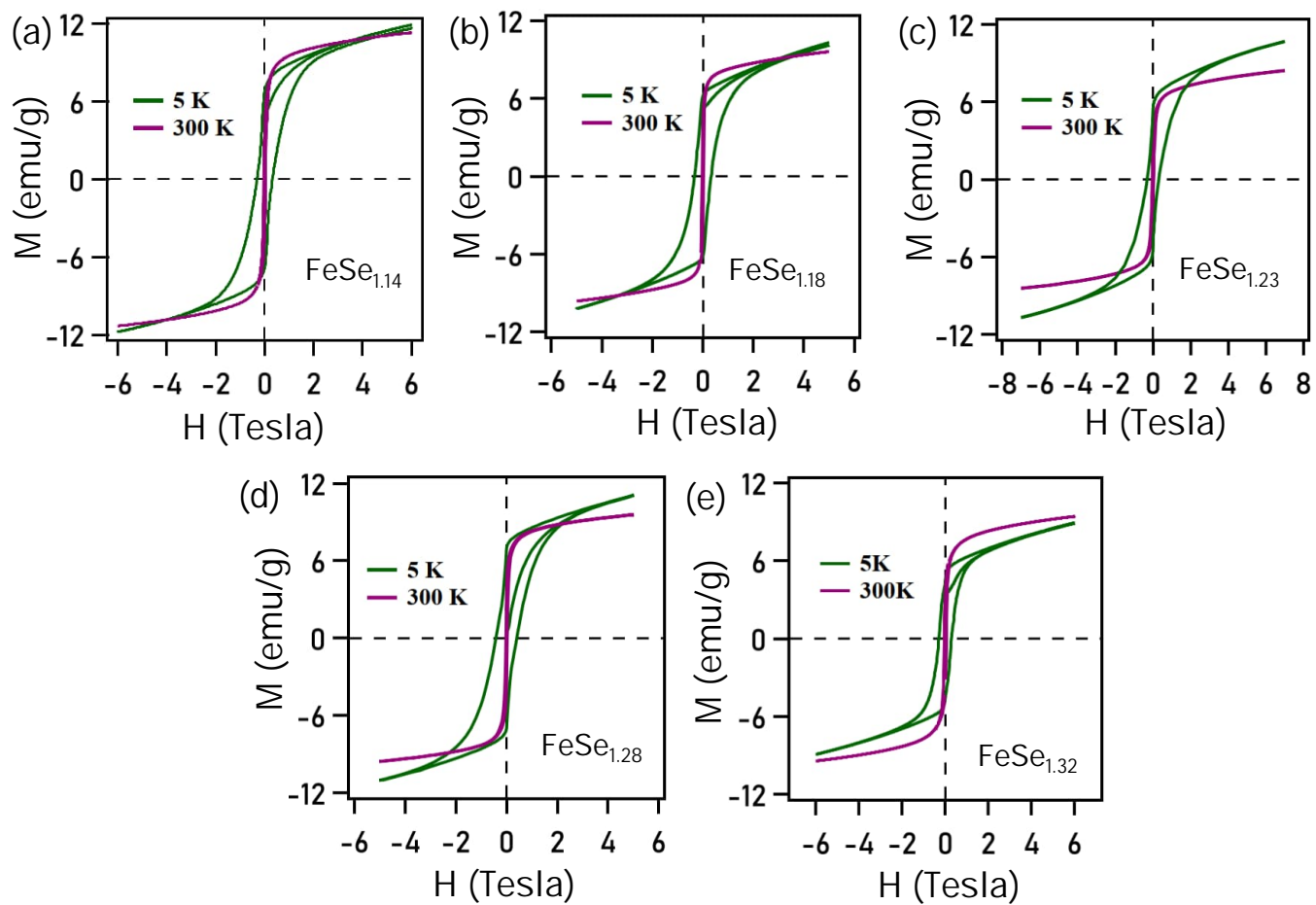


FIG. 11. Fig. S4: Magnetization as a function of field [$M(H)$] recorded at 5 and 300 K for FeSe_x ($x = 1.14, 1.18, 1.23, 1.28,$ and 1.32).

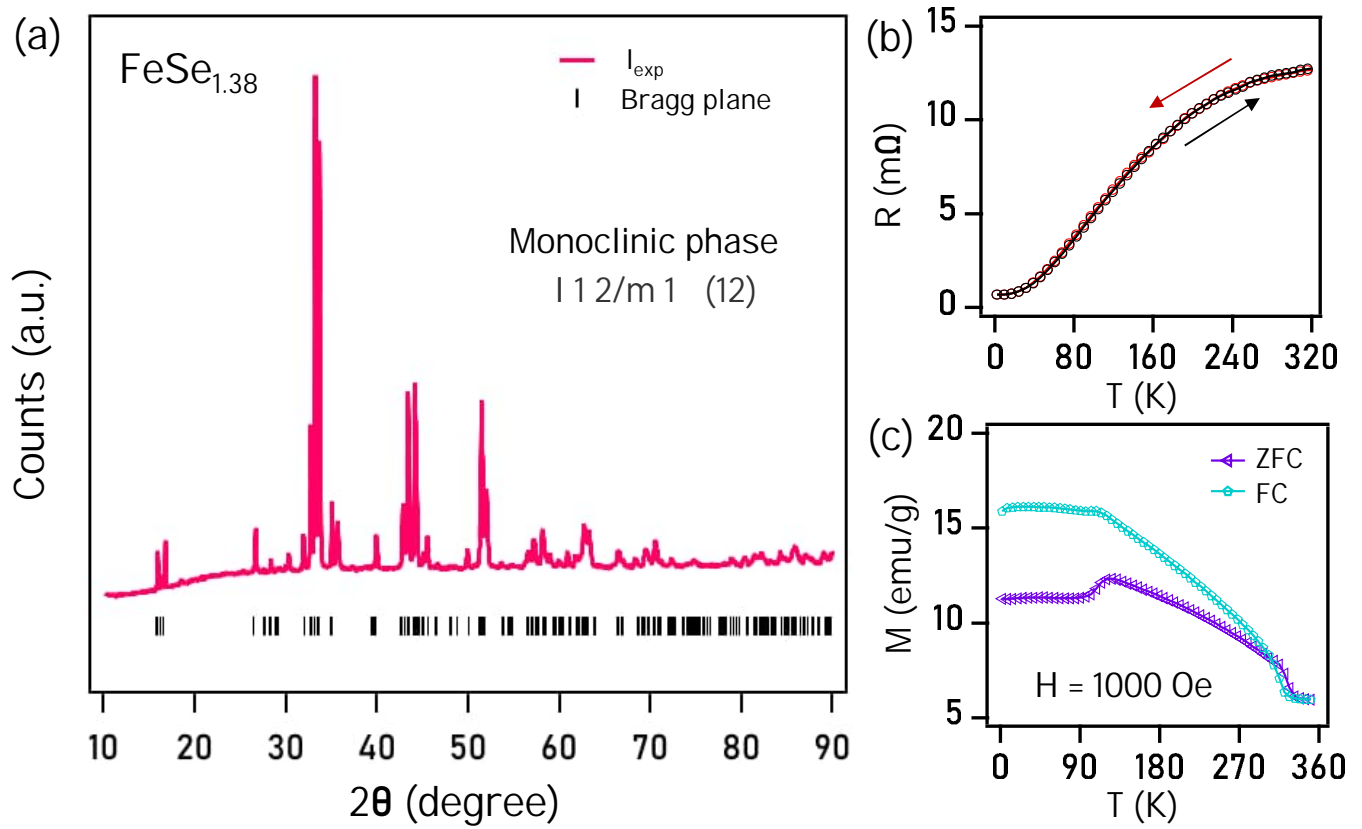


FIG. 12. Fig. S5:(a) Powder X-ray diffraction pattern taken at room temperature on $\text{FeSe}_{1.38}$. (b) Temperature-dependent resistance measured during both heating and cooling cycles (absence of hysteresis in the resistance data suggest absence of structural changes in $\text{FeSe}_{1.38}$ between 2 and 350 K). (c) Magnetization as a function of temperature under zero-field-cooling (ZFC) and field-cooling (FC) modes with an applied field of 1000 Oe. In (c), the spin-reorientation transition is found at around 112 K.